Project 039 Naphthalene Removal Assessment

Massachusetts Institute of Technology

Project Lead Investigator

Prof. Steven R. H. Barrett
Leonardo Associate Professor of Aeronautics and Astronautics
Department of Aeronautics and Astronautics
Massachusetts Institute of Technology
77 Massachusetts Avenue – Bldg. 33-316
Cambridge, MA 02139
(617)-452-2550
sbarrett@mit.edu

University Participants

Massachusetts Institute of Technology

- PIs: Prof. Steven R. H. Barrett and Dr. Raymond Speth (Co-PI)
- FAA Award Number: 13-C-AJFE-MIT, Amendment Nos. 026, 034, 043, and 053
- Period of Performance: July 8, 2016 to February 28, 2021 (with the exception of funding and cost share information, this report covers the period from October 1, 2019 to September 30, 2020)
- Tasks:
    1. Evaluate changes in emissions resulting from removal of naphthalene.
    2. Conduct integrated cost-benefit analysis of impacts of naphthalene removal in the United States.

Project Funding Level

The funding comprises $840,000 in FAA funding and $840,000 in matching funds. Sources of match are approximately $233,000 from the Massachusetts Institute of Technology (MIT), plus third-party in-kind contributions of $361,000 from Oliver Wyman Group and $246,000 from Byogy Renewables, Inc.

Investigation Team

- Prof. Steven Barrett (MIT) serves as PI for ASCENT Project 39 as head of the Laboratory for Aviation and the Environment. Prof. Barrett both coordinates internal research efforts and maintains communication among investigators in the various MIT research teams mentioned below.
- Dr. Raymond Speth (MIT) serves as co-PI for ASCENT Project 39. Dr. Speth directly advises students performing research in the Laboratory for Aviation and the Environment, with a focus on assessment of naphthalene removal refinery options; climate and air quality modeling; and fuel alteration life-cycle analysis. Dr. Speth also coordinates communication with FAA counterparts.
- Prof. William Green (MIT) serves as a co-investigator for ASCENT Project 39, as head of the Green Research Group. Prof. Green advises students on work in the Green Research Group focused on computer-aided chemical kinetic modeling of polycyclic aromatic hydrocarbon (PAH) formation.
- Mr. Randall Field (MIT) is the Executive Director of the MIT Energy Initiative and a co-investigator ASCENT Project 39. Drawing upon his experiences as a business consulting director at Aspen Technology Inc., Mr. Field provides mentorship to student researchers in the selection and assessment of naphthalene removal refining options and process engineering at large.
- Mr. Drew Weibel (MIT) was a graduate student researcher in the Laboratory for Aviation and the Environment. Mr. Weibel was responsible for conducting selection and assessment of naphthalene removal refining options; calculation of refinery process requirements and fuel composition effects from selected processes; estimation of capital and operating costs of naphthalene removal processes; air quality and climate modeling; and integrated cost-benefit analysis.

- Mr. Lukas Brink (MIT) is a graduate student researcher in the Laboratory for Aviation and the Environment. Mr. Brink is responsible for the development of a combustor model quantifying the effect of naphthalene removal on soot emissions, the modeling of air quality and climate impacts, and integrated cost-benefit analysis.

Project Overview

Aircraft emissions impact the environment by perturbing the climate and reducing air quality, thus leading to adverse health impacts including an increased risk of premature mortality. As a result, understanding how different fuel components can influence pollutant emissions, as well as the resulting impacts and damage to human health and the environment, is important in guiding future research aims and policy. Recent emissions measurements have shown that removal of naphthalenes can dramatically decrease emissions of particulate matter (Brem et al., 2015; Moore et al., 2015). The objective of this research is to determine the benefits, costs, and feasibility of removing naphthalenes from jet fuel, with regard to the refiner, the public, air quality, and the environment. Specific goals of this research include:

- Assessment and selection of candidate refining processes for the removal of naphthalenes from conventional jet fuel, including details of required technology, steady-state public cost, and changing life-cycle emissions impacts at the refinery.
- Development of a chemical kinetics model to better understand the link between fuel aromatic composition and the resulting particulate matter (PM) emissions due to jet fuel combustion.
- Assessment of the climate and air quality impacts associated with naphthalene reduction and/or removal from jet fuel.
- Development of a life-cycle analysis of the relative costs of removing naphthalene from jet fuel and the associated benefits due to avoided premature mortalities and climate damage for a range of possible scenarios.

References

Brem, B.T., Durdina, L., Siegerist, F., Beyerle, P., Bruderer, K., Rindlisbacher, T., Rocci-Denis, S., Andac, M.G., Zelina, J., Penanhoat, O., & Wang, J. (2015). Effects of fuel aromatic content on nonvolatile particulate emissions of an in-production aircraft gas turbine. Environmental Science and Technology 49 13149–57

Moore, R.H., Shook, M., Beyersdorf, A., Corr, C., Herndon, S., Knighton, W.B., Miake-Lye, R., Thornhill, K.L., Winstead, E.L., Yu, Z., Ziemba, L.D. & Anderson, B.E. (2015). Influence of jet fuel composition on aircraft engine emissions: A synthesis of aerosol emissions data from the NASA APEX, AAFEX, and ACCESS missions. Energy Fuels 29 2591–600

Task 1 – Evaluate Changes in Emissions Resulting from Removal of Naphthalene

Massachusetts Institute of Technology

Objective

Changes to jet fuel composition, such as those achieved by removal of naphthalene using available refining technologies, affect the chemical kinetics of the combustion process in gas turbine engines, which in turn affects the resulting emissions. To enable evaluation of the sensitivity of soot emissions to fuel composition, this Task develops a combustor model that includes the detailed chemical kinetic pathways for formation of polycyclic aromatic hydrocarbon (PAH) species from different fuel components and the conversion of these PAH species to soot particles or non-volatile particulate matter (nvPM) emissions. The model also provides the ability to predict changes to CO and NO_x emissions resulting from changes to fuel composition.

Research Approach

The aircraft engine emissions model developed here has three main components: a soot model, an engine model, and a combustor model. The combustor model consists of a reactor network coupled with a gas-phase kinetic mechanism, which is modeled using Cantera (Goodwin et al., 2018). A soot model is added to the reactor network and the interactions between the gas phase and the solid soot phase are modeled in detail. The altitude- and thrust-specific input conditions for the combustor are generated with the engine model. The model is called Pycaso (Python Cantera Soot). The model is used to predict emissions for a CFM56-7B/3 engine because it is one of the most prevalent engines in the commercial fleet, and measurement data for soot emissions from this engine have been published.

Soot model

Due to the uncertainty in soot modeling in gas turbine combustors, a two-equation model is used, which captures all the major soot formation and depletion processes while minimizing complexity. In a two-equation model, the soot number density (N) and mass density (M) are modeled using two equations, which represent the change in soot N and M in response to four soot formation and depletion steps. The standard two-equation model assumes that oxidation solely affects M and does not directly destroy soot particles. However, experiments have shown that oxidation can destroy particles and can thus reduce N (Garo et al., 1988; Lindstedt, 1994). Therefore, an additional term is included in the number density equation to capture the effect of particle destruction through oxidation. It is assumed that for every change in soot mass equivalent to the average soot particle mass, a variable fraction of a particle is destroyed as well. The resulting equations for N and M are

$$\frac{dN}{dt} = C_{\text{nuc}}\left(\frac{dN}{dt}\right)_{\text{nuc}} + C_{\text{coag}}\left(\frac{dN}{dt}\right)_{\text{coag}} + C_{\text{ox},N}\frac{N}{M}C_{\text{ox}}\left(\frac{dM}{dt}\right)_{\text{ox}}, \tag{1}$$

and

$$\frac{dM}{dt} = C_{\text{nuc}}\left(\frac{dM}{dt}\right)_{\text{nuc}} + C_{\text{sg}}\left(\frac{dM}{dt}\right)_{\text{sg}} + C_{\text{ox}}\left(\frac{dM}{dt}\right)_{\text{ox}}. \tag{2}$$

During nucleation, the inception of soot particles happens through collisions of precursor species (Blanquart & Pitsch, 2009). These precursor species are considered to primarily consist of heavy PAH molecules (Dobbins et al., 1998; Schuetz & Frenklach, 2002). When two PAH molecules collide and stick together, they form a PAH dimer, which again increases in size through collisions with other PAH species and dimers. This growth through collisions allows for transitioning from the gas phase to the solid phase and results in the first solid incipient soot particle (Martini, 2008). PAH-PAH collision rates are considered for nucleation in the model, while PAH-soot collisions are modeled as surface growth. The nucleation rate resulting from collisions of PAH species i and j is based on the collision frequency $\beta i,j$ and is given by

$$\left(\frac{dN}{dt}\right)_{\text{nuc},ij} = \frac{\gamma_i + \gamma_j}{2}\varepsilon\sqrt{\frac{8\pi k_B T}{\mu_{i,j}}}N_A^2\left(r_i + r_j\right)^2[\text{PAH}_i][\text{PAH}_j], \tag{3}$$

where ε = 2.2 is the Van der Waals enhancement factor, k_B is the Boltzmann constant, N_A is Avogadro's constant, r_i and r_j are the radii of PAH species i and j, $\mu_{i,j}$ is the reduced mass of PAH species i and j, and $[\text{PAH}_i]$ is the concentration of PAH species i (An et al., 2016; Atkins et al., 2018; Blanquart & Pitsch, 2009). The sticking coefficient $\gamma < 1$ is computed using the assumption that it scales with PAH mass to the fourth power (Blanquart & Pitsch, 2009). The PAH species are chosen such that no direct pathways from species in the fuel surrogates to soot mass through nucleation exist, as these pathways might result in an overestimation of sensitivities to fuel composition. The total nucleation rate is calculated by taking the sum over all the PAH species in the gas-phase mechanism.

Nucleation is followed by surface growth and coagulation. During surface growth, the soot particles grow in size and mass due to the adsorption of gas phase molecules, mainly acetylene (Omidvarborna et al., 2015). Growth rates are found to be much higher than nucleation rates and most of the soot mass is thought to form during this step in the process (Martini, 2008). Here, two types of surface growth mechanisms are implemented. The first assumes surface growth solely by acetylene, whereas the second also includes surface growth through condensation of PAH species on the soot surface. In order to include surface growth through the adsorption of PAH species, the surface growth source term is expanded with an additional term. This term is based on the collision frequency of soot particles with PAH species i and is given by

$$\left(\frac{dM}{dt}\right)_{\text{sg,PAH}} = \sum_{i=1}^{L} n_{\text{C},i}W_{\text{C}}\frac{\gamma_i + \gamma_{soot}}{2}\varepsilon\sqrt{\frac{8\pi k_B T}{\mu_{\text{soot},i}}}\left(r_i + \frac{d_p}{2}\right)^2[\text{PAH}_i]N. \tag{4}$$

Since this term is similar to the nucleation term, it is scaled with C_{nuc} instead of C_{sg}.

During coagulation, soot particles grow further in size through particle-particle collisions (Blanquart & Pitsch, 2009; Omidvarborna et al., 2015). The total number of soot particles decreases during coagulation whereas the total mass across all particles stays constant. The implemented coagulation mechanism is based on the collision of two spherical particles with a collision rate as defined by Puri et al. (1993). The resulting source term for the number density equation is given by

$$\left(\frac{dN}{dt}\right)_{\text{coag}} = -K_{\text{coag}}\sqrt{\frac{24R_uT}{\rho_{\text{soot}}N_A}}\sqrt{d_p}N^2, \tag{5}$$

where ρ_{soot} is assumed to be equal to 2000 kg/m^3 and K_{coag} is a constant ranging between 1 and 9 in the literature (Brookes & Moss, 1999; Wen et al., 2003).

In contrast to the previous three steps, soot is destroyed during oxidation. Oxidation significantly reduces the amount of soot and measurements suggest that most of the soot formed at the start of the combustion process is oxidized before reaching the combustor exit (Toone, 1968). Carbon and hydrogen atoms are removed from the soot agglomerates by reactions with primarily diatomic oxygen (O_2), hydroxyl radicals (OH), and atomic oxygen (O) (Louloudi, 2003; Neoh et al., 1981). Their respective contributions to the oxidation source term (Guo et al., 2016; Martini, 2008; Schiener & Lindstedt, 2018) are given by

$$\left(\frac{dM}{dt}\right)_{\text{ox},O_2} = -745.88\eta_{O_2}W_C\sqrt{T}\exp\left(-\frac{19{,}680}{T}\right)[O_2]A_s, \tag{6}$$

and

$$\left(\frac{dM}{dt}\right)_{\text{ox,OH}} = -\eta_{\text{OH}}W_C\sqrt{T}[\text{OH}]A_{s,} \tag{7}$$

and

$$\left(\frac{dM}{dt}\right)_{\text{ox,O}} = -1.82\eta_O W_C\sqrt{T}[O]A_s, \tag{8}$$

where the collision efficiencies for O_2 and O (η_{O_2} and η_O) are assumed to be unity (Mueller et al., 2009; Wen et al., 2003). For oxidation through OH, collision efficiency values ranging from 0.01 to 0.65 have been proposed (Fenimore & Jones, 1967; Ghiassi et al., 2017; Guo et al., 2016; Haudiquert et al., 1997; Neoh et al., 1981; Puri et al., 1994; Richter et al., 2005; Schiener & Lindstedt, 2018). We use a value of 0.13, determined by Neoh et al. (1981), as baseline value in this model.

Engine model

The combustor inlet temperature (T_3) and pressure (P_3), as well as the mass flows of fuel ($\dot{m}_{\text{fuel}}$) and air ($\dot{m}_{\text{air}}$) entering the combustor are computed using a detailed engine model of the CFM56-7B engine. The engine model is developed using the Numerical Propulsion System Software (NPSS) and matches fuel flows, thrust levels, and pressure ratios from the International Civil Aviation Organization (ICAO) engine Emissions Databank (EDB) within 5%. The temperature of the gas-phase mixture entering the combustor is corrected for vaporization of the fuel by adjusting the specific enthalpy of the gas-fuel mixture as follows:

$$h_{\text{mix}} = \frac{1}{\dot{m}_{\text{air}}}\left[\dot{m}_{\text{air}}h_{\text{air},P_3T_3} + \dot{m}_{\text{fuel}}h_{\text{fuel},P_3T_3} - \dot{m}_{\text{fuel}}(L + \Delta h)\right], \tag{9}$$

where L represents the enthalpy of vaporization at standard conditions (T =298.15 K and P = 101,325 Pa), h is the specific enthalpy, and Δh is the change in specific enthalpy going from standard conditions to T_3 and P_3. $\dot{m}_{\text{fuel}}$ and $\dot{m}_{\text{air}}$ are the mass flow rates of fuel and air, respectively.

Combustor model

The combustor model developed for this project represents a rich-burn quick-mix lean-burn (RQL) combustor. Figure 1 shows a schematic overview of the model. The model is divided into two parts called the primary zone and the secondary zone. In the primary zone, air and fuel are mixed at a certain equivalence ratio. Then, the quenching happens at the start of the secondary zone through to the addition of secondary air in the slow and fast mixing zones. In the second part of the secondary zone, dilution air is added to represent the lean burn zone. As NO_x, CO, and soot reactions are found to be quenched at the end of the secondary zone, the turbine is not modeled. The gas phase chemistry inside the combustor model is modeled using a kinetic mechanism which determines the structure of the flame and specifies the species profile

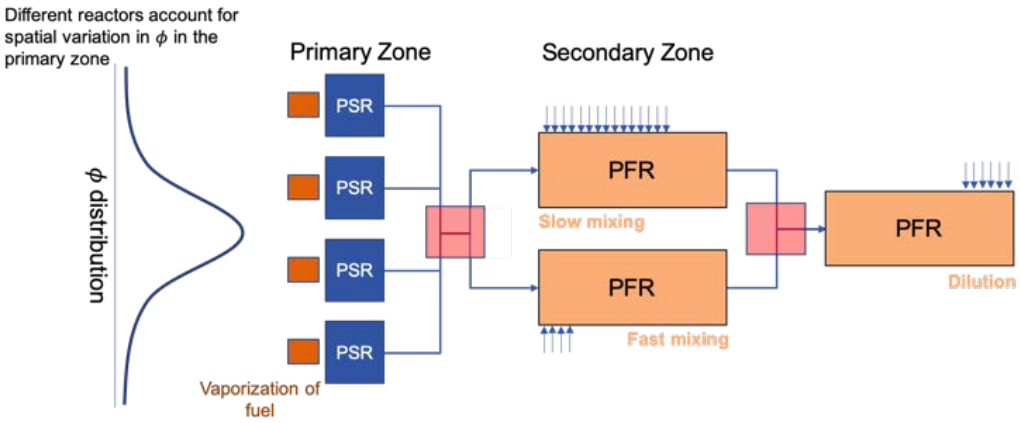

Figure 1. Schematic overview of the combustor model. Multiple well-stirred reactors (WSR) are used in the primary zone. The secondary zone uses a combination of plug flow reactors (PFR) to simulate different mixing times. The arrows represent secondary and dilution air entering the combustor.

(Appel et al., 2000). A high temperature kinetic mechanism for transportation fuels is coupled with a NO_x mechanism, resulting in a chemical mechanism consisting of 218 species and 7047 reactions (Ranzi et al., 2012, 2014, 2015).

The combustor model can be used to represent different (RQL) combustors. In order to represent a specific combustor design, combustor model parameters are calibrated using emissions data from the EDB for an engine containing that specific combustor. Since the combustor model can be considered a "black box" function and obtaining a (numerical) gradient is computationally expensive, gradient-free optimization is used to calibrate the model parameters. More specifically, the DIvided RECTangles (DIRECT) method is applied (Finkel, 2003; Hicken et al., 2012; Jones, 2009).

Milestones

The combined combustor, soot, and engine model described above were implemented, and used to explore the impact of different jet fuel compositions on NO_x, CO, and soot emissions.

Major Accomplishments

Model validation

Eight different soot model configurations (C1–C8) were developed. Each configuration consists of a different set of reaction rate coefficients and/or soot mechanisms. These eight configurations are selected in order to capture a range of soot mechanisms in literature and to quantify the impact and behavior of each step of the soot formation process. The performance of the configurations against measurements for both emission index (EI) mass and number is summarized in Figure 2. Starting with EI soot mass, two clusters of configurations are visible. Configurations 1–5 capture the trends in the validation data for thrust levels >= 30%. On the other hand, configurations 6–8 capture the trend in the data for thrust settings larger than approximately 75% but underpredict soot mass emissions thrust settings lower than 75%. For soot number EI, the models all capture the trend in the validation data of decreasing number EI with increasing thrust between approximately 60% and 100% thrust. Configurations 4, 5, and 6 also capture the 30% thrust point, whereas configurations 1, 2, 7, and 8 underpredict soot number at this thrust setting, while configuration 3 overpredicts it.

We find that primary zone soot mass formation peaks at $\varphi \approx 2.3$, where the EI soot is approximately seven times higher than at $\varphi \approx 3.0$ and $\varphi \approx 2.0$. On the other hand, soot number increases with equivalence ratio and peak EI soot number values are observed in the richest reactors. This difference is explained by the PAH concentration being the limiting factor for nucleation (soot number), whereas temperature and C_2H_2 concentration are the limiting factors for soot mass (surface growth).

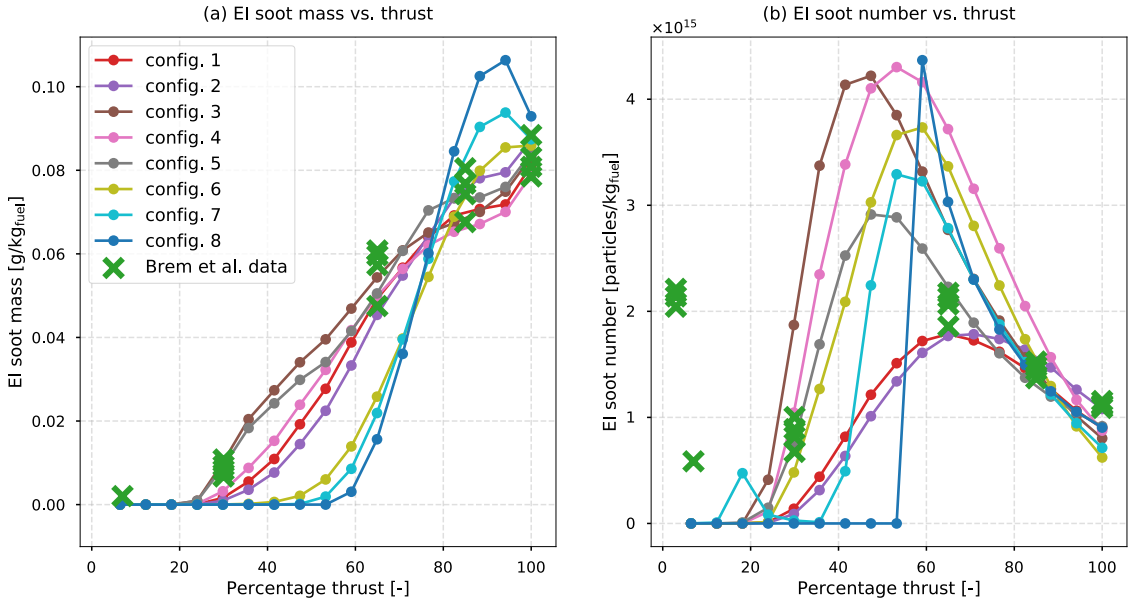

Figure 2. Comparison of EI soot (a) mass and (b) number with validation data (surrogate 4).

In order to validate the model's capability to predict changes in soot emissions in response to changing fuel compositions, we simulate a subset of the experiments conducted by Brem et al. (2015) where soot emissions are measured for two fuel blends with different naphthalene and aromatic content. The soot predictions of each of the model configurations for two versions of each of the five surrogates are evaluated. The total aromatics % v/v, naphthalene % v/v, and hydrogen content of these two fuels match the values used in experiments by Brem et al. (2015). The resulting changes in EI soot mass and number are shown in Figure 3. We see that the three configurations using the hydrogen abstraction acetylene addition (HACA) mechanisms show large discrepancies for both soot mass and number. The five other configurations can be grouped based on their values for C_{coag} and $C_{\mathrm{ox},N}$. The three configurations (1, 2, and 4) with relatively low coagulation factors (<30) and relatively large $C_{\mathrm{ox},N}$ values (> 0.65) match the soot mass data from Brem et al. (2015) within 5 percentage points (p.p.) at 30% and 65% thrust, 8 p.p. at 85% thrust, and 18 p.p. at 100% thrust, and within 15 p.p. of the soot number data for all thrust conditions. When increasing the coagulation factor and decreasing $C_{\mathrm{ox},N}$ (configurations 3 and 5), these differences grow to a maximum of 51 p.p. at 100% thrust for configuration 5. A possible explanation for the relatively large discrepancies at high thrust for the configuration using high coagulation factors is that these configurations rely on a large N in the primary zone (PZ) to increase the average particle size (and thus the M/A_s ratio). When reducing the naphthalene content of the fuel, less nucleation occurs and the soot number density decreases. This again reduces coagulation and increases M/A_s which leads to more oxidation in the secondary zone. On the other hand, configurations relying on $C_{\mathrm{ox},N}$ to reduce N are not affected as much by a decreasing N. Due to their superior performance compared on the validation data, configurations 1, 2, and 4 are selected to assess the sensitivity of soot to naphthalene removal and biofuels in the subsequent analysis of fuel composition effects.

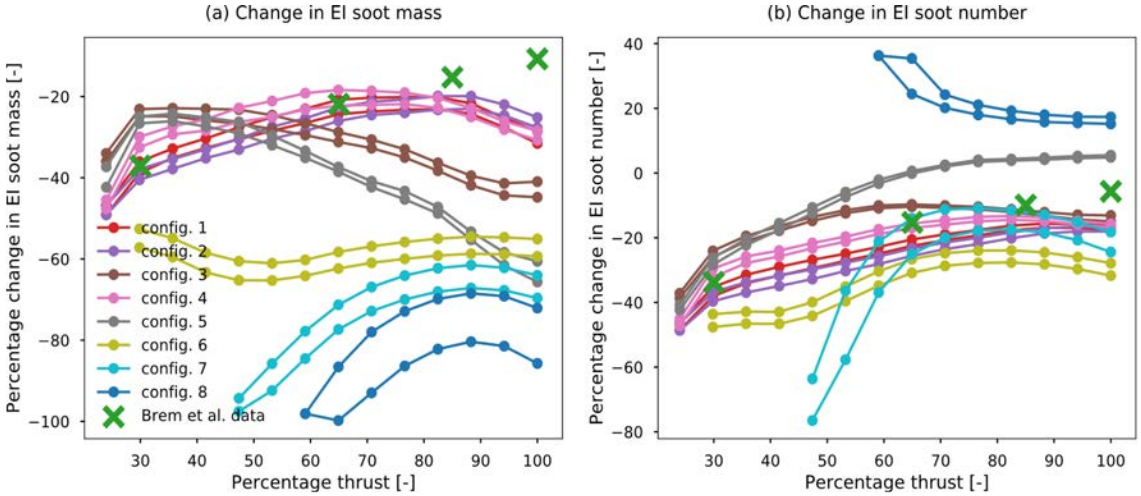

Figure 3. Comparison of model predictions with experimental data by Brem et al. (2015). Percentage change in EI soot (a) mass and (b) number for all eight configurations.

Effects of fuel composition

Figure 4 shows the computed ranges of soot mass and number emissions reductions associated with the naphthalene removal through extractive distillation and hydrotreating. These ranges represent both variations in the three soot model configurations as well as the five baseline fuel compositions. The mean reductions in EI mass are approximately 20 p.p. higher for extractive distillation than for hydrotreating. For EI soot number, the differences between the means of the two methods range from 12 p.p. at 100% thrust to 28 p.p. at 30% thrust. These differences are explained by tetralin, the product of hydrotreating naphthalene, still being an aromatic species and having a relatively short pathway to becoming a PAH species during combustion. Reductions in mass are predicted to be larger than reductions in number (for >35% thrust), which is consistent with the literature (Brem et al., 2015; Speth et al., 2015).

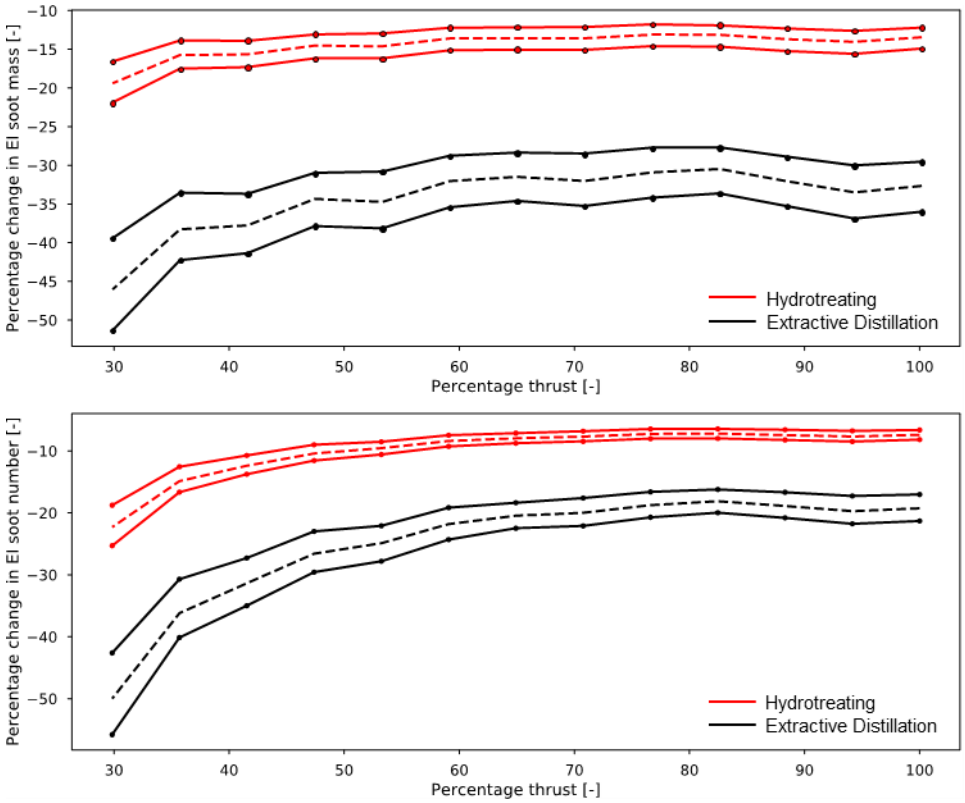

Figure 4. Ranges of predicted effects of naphthalene removal from jet fuel by hydrotreating (red) and extractive distillation (black) on EI soot (a) mass and (b) number emissions indices. The dashed lines represent the means of the prediction ranges, which capture variations in three different soot configurations and five different surrogates.

Furthermore, especially for number emissions, reductions increase with decreasing thrust. This effect is also observed in experiments in the literature (Brem et al., 2015; Corporan et al., 2007; Naegeli & Moses, 2015; Speth et al., 2015). We find that the increasing change in soot emissions with decreasing thrust is explained by two main factors. The first one is that sensitivity to fuel composition increases with decreasing PZ equivalence ratio. The changes in EI soot mass and number due to naphthalene removal are found to be approximately 1.5 and 2–3 times higher at φ=2.2 compared to φ=3.0, respectively. The lower the thrust setting, the lower the primary zone equivalence ratio(s), and thus the higher the sensitivity to fuel composition. The second factor is that for a given φ, the reductions in both soot mass and number increase with decreasing thrust. This is explained by the temperature difference between the thrust conditions. Higher temperatures at higher thrust settings make the reactor more resilient to changes in naphthalene concentrations.

Figure 5 shows the predicted effects of using 20%, 50%, and 100% biofuel blends on soot emissions. As expected, mean reductions increase with increasing the biofuel fraction and decreasing thrust. The predicted reductions for soot mass range from 17%, 37%, and 55% at 100% thrust to 25%, 56%, and 92% at 30% thrust. For soot number, mean reductions at 100% thrust are 11%, 26%, and 51% compared to reductions of 24%, 56%, and 92% at 30% thrust.

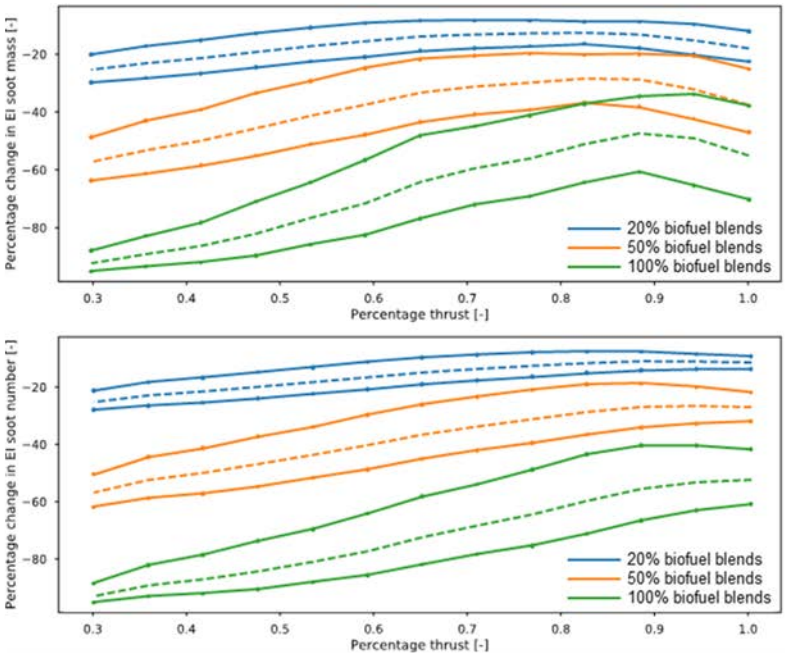

Figure 5. Effects of using 20% (blue), 50% (orange) and 50% (green) biofuel blends on EI soot (a) mass and (b) number. The dashed lines represent the means of the prediction ranges, which capture variations in three different soot mechanisms and five different surrogates.

The effect of using 20%, 50%, and 100% biofuel blends on NO_x and CO emissions is shown in Figure 6. The model predicts mean reductions in NO_x emissions of 2%, 5%, and 10% and reductions in CO emissions of 1%, 2%, and 5% for the three blends, respectively. The sharp drop in CO at the lowest thrust setting is a consequence of the finite number of reactors in the model and the corresponding CO values are therefore not considered. This sharp drop in CO occurs because the leanest reactor blows out for the standard surrogate and does not for the 50% and 100% biofuel blends. This leads to an increase in secondary zone (SZ) mixing temperature and thus CO depletion.

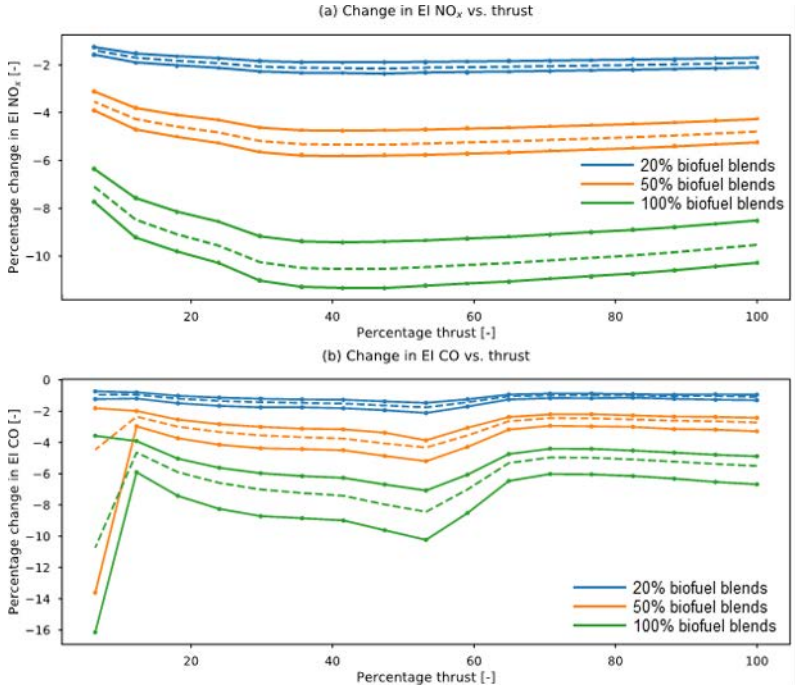

Figure 6. Effects of using 20% (blue), 50% (orange) and 100% (green) biofuel blends on (a) NO_x and (b) CO emissions. The dashed lines represent the means of the prediction ranges, which capture variations in five different surrogates.

Publications
N/A

Outreach Efforts
The results of this work were presented at the Aviation Emissions Characterization (AEC) Roadmap annual meeting held in May 2020.

Awards
None.

Student Involvement
This task was conducted primarily by Lukas Brink, working directly with Prof. Steven Barrett and Dr. Raymond Speth. Mr. Brink graduated with a Master of Science in 2020.

Plans for Next Period
Task is complete. A journal paper based on this work is being prepared for submission.

References
An, Y., Li, X., Teng, S., Wang, K., Pei, Y., Qin, J., & Zhao, H. (2016). Development of a soot particle model with PAHs as precursors through simulations and experiments. *Fuel*, *179*, 246–257. https://doi.org/10.1016/j.fuel.2016.03.100

Appel, J., Bockhorn, H., & Frenklach, M. (2000). Kinetic modeling of soot formation with detailed chemistry and physics: Laminar premixed flames of C_2 hydrocarbons. *Combustion and Flame*, *121*(1–2), 122–136.

Atkins, P. W., De Paula, J., & Keeler, J. (2018). *Atkins' physical chemistry*. Oxford University Press.

Blanquart, G., & Pitsch, H. (2009). A joint volume-surface-hydrogen multi-variate model for soot formation. *Combustion Generated Gine Carbonaceous Particles*, 437–463.

Brookes, S. J., & Moss, J. B. (1999). Predictions of soot and thermal radiation properties in confined turbulent jet diffusion flames. *Combustion and Flame*, *116*(4), 486–503. https://doi.org/10.1016/S0010-2180(98)00056-X

Corporan, E., DeWitt, M. J., Belovich, V., Pawlik, R., Lynch, A. C., Gord, J. R., & Meyer, T. R. (2007). Emissions Characteristics of a Turbine Engine and Research Combustor Burning a Fischer–Tropsch Jet Fuel. *Energy & Fuels*, *21*(5), 2615–2626. https://doi.org/10.1021/ef070015j

Dobbins, R. A., Fletcher, R. A., & Chang, H.-C. (1998). The evolution of soot precursor particles in a diffusion flame. *Combustion and Flame*, *115*(3), 285–298. https://doi.org/10.1016/S0010-2180(98)00010-8

Fenimore, C. P., & Jones, G. W. (1967). Oxidation of soot by hydroxyl radicals. *The Journal of Physical Chemistry*, *71*(3), 593–597. https://doi.org/10.1021/j100862a021

Finkel, D. (2003). *DIRECT optimization algorithm user guide*. North Carolina State University. Center for Research in Scientific Computation.

Garo, A., Lahaye, J., & Prado, G. (1988). Mechanisms of formation and destruction of soot particles in a laminar methane-air diffusion flame. *Symposium (International) on Combustion*, *21*(1), 1023–1031. https://doi.org/10.1016/S0082-0784(88)80333-3

Ghiassi, H., Lignell, D., & Lighty, J. S. (2017). Soot Oxidation by OH: Theory Development, Model, and Experimental Validation. *Energy & Fuels*, *31*(3), 2236–2245. https://doi.org/10.1021/acs.energyfuels.6b02193

Goodwin, D. G., Speth, R. L., Moffat, H. K., & Weber, B. W. (2018). *Cantera: An object-oriented software toolkit for chemical kinetics, thermodynamics, and transport processes.* Version 2.4.0. https://www.cantera.org.

Guo, H., Anderson, P. M., & Sunderland, P. B. (2016). Optimized rate expressions for soot oxidation by OH and O2. *Fuel*, *172*, 248–252. https://doi.org/10.1016/j.fuel.2016.01.030

Haudiquert, M., Cessou, A., Stepowski, D., & Coppalle, A. (1997). OH and soot concentration measurements in a high-temperature laminar diffusion flame. *Combustion and Flame*, *111*(4), 338–349. https://doi.org/10.1016/S0010-2180(97)00003-5

Hicken, J., Alonso, J., & Farhat, C. (2012). *Introduction to multidisciplinary design optimization: Chapter 6: Gradient-free optimization*. Stanford University.

Jones, D. R. (2009). Direct global optimization algorithm. *Encyclopedia of Optimization*, *1*(1), 431–440.

Lindstedt, P. R. (1994). Simplified Soot Nucleation and Surface Growth Steps for Non-Premixed Flames. In H. Bockhorn (Ed.), *Soot Formation in Combustion: Mechanisms and Models* (pp. 417–441). Springer. https://doi.org/10.1007/978-3-642-85167-4_24

Louloudi, S. (2003). *Transported probability density function: Modelling of turbulent jet flames*. Imperial College London (University of London).

Martini, B. (2008). *Development and assessment of a soot emissions model for aircraft gas turbine engines* [Thesis, Massachusetts Institute of Technology]. https://dspace.mit.edu/handle/1721.1/45256

Mueller, M. E., Blanquart, G., & Pitsch, H. (2009). Hybrid Method of Moments for modeling soot formation and growth. *Combustion and Flame*, *156*(6), 1143–1155. https://doi.org/10.1016/j.combustflame.2009.01.025

Naegeli, D. W., & Moses, C. A. (2015, April 17). *Effect of Fuel Molecular Structure on Soot Formation in Gas Turbine Engines*. ASME 1980 International Gas Turbine Conference and Products Show. https://doi.org/10.1115/80-GT-62

Neoh, K. G., Howard, J. B., & Sarofim, A. F. (1981). Soot Oxidation in Flames. In D. C. Siegla & G. W. Smith (Eds.), *Particulate Carbon: Formation During Combustion* (pp. 261–282). Springer US. https://doi.org/10.1007/978-1-4757-6137-5_9

Omidvarborna, H., Kumar, A., & Kim, D.-S. (2015). Recent studies on soot modeling for diesel combustion. *Renewable and Sustainable Energy Reviews*, *48*, 635–647. https://doi.org/10.1016/j.rser.2015.04.019

Puri, R., Richardson, T. F., Santoro, R. J., & Dobbins, R. A. (1993). Aerosol dynamic processes of soot aggregates in a laminar ethene diffusion flame. *Combustion and Flame*, *92*(3), 320–333.

Puri, R., Santoro, R. J., & Smyth, K. C. (1994). *Oxidation of Soot and Carbon Monoxide in Hydrocarbon Diffusion Flames*. *97*, 125–144.

Ranzi, E., Cavallotti, C., Cuoci, A., Frassoldati, A., Pelucchi, M., & Faravelli, T. (2015). New reaction classes in the kinetic modeling of low temperature oxidation of n-alkanes. *Combustion and Flame*, *162*(5), 1679–1691. https://doi.org/10.1016/j.combustflame.2014.11.030

Ranzi, E., Frassoldati, A., Grana, R., Cuoci, A., Faravelli, T., Kelley, A. P., & Law, C. K. (2012). Hierarchical and comparative kinetic modeling of laminar flame speeds of hydrocarbon and oxygenated fuels. *Progress in Energy and Combustion Science*, *38*(4), 468–501. https://doi.org/10.1016/j.pecs.2012.03.004

Ranzi, E., Frassoldati, A., Stagni, A., Pelucchi, M., Cuoci, A., & Faravelli, T. (2014). Reduced Kinetic Schemes of Complex Reaction Systems: Fossil and Biomass-Derived Transportation Fuels. *International Journal of Chemical Kinetics*, *46*(9), 512–542. https://doi.org/10.1002/kin.20867

Richter, H., Granata, S., Green, W. H., & Howard, J. B. (2005). Detailed modeling of PAH and soot formation in a laminar premixed benzene/oxygen/argon low-pressure flame. *Proceedings of the Combustion Institute*, *30*(1), 1397–1405. https://doi.org/10.1016/j.proci.2004.08.088

Schiener, M. A., & Lindstedt, R. P. (2018). Joint-scalar transported PDF modelling of soot in a turbulent non-premixed natural gas flame. *Combustion Theory and Modelling*, *22*(6), 1134–1175. https://doi.org/10.1080/13647830.2018.1472391

Schuetz, C. A., & Frenklach, M. (2002). Nucleation of soot: Molecular dynamics simulations of pyrene dimerization. *Proceedings of the Combustion Institute*, *29*(2), 2307–2314. https://doi.org/10.1016/S1540-7489(02)80281-4

Speth, R. L., Rojo, C., Malina, R., & Barrett, S. R. H. (2015). Black carbon emissions reductions from combustion of alternative jet fuels. *Atmospheric Environment*, *105*, 37–42. https://doi.org/10.1016/j.atmosenv.2015.01.040

Toone, B. (1968). A Review of Aero Engine Smoke Emission. In I. E. Smith (Ed.), *Combustion in Advanced Gas Turbine Systems* (pp. 271–296). Pergamon. https://doi.org/10.1016/B978-0-08-013275-4.50019-2Wen, Z., Yun, S., Thomson, M. J., & Lightstone, M. F. (2003). Modeling soot formation in turbulent kerosene/air jet diffusion flames. *Combustion and Flame*, *135*(3), 323–340. https://doi.org/10.1016/S0010-2180(03)00179-2

Wen, Z., Yun, S., Thomson, M. J., & Lightstone, M. F. (2003). Modeling soot formation in turbulent kerosene/air jet diffusion flames. *Combustion and Flame*, *135*(3), 323–340. https://doi.org/10.1016/S0010-2180(03)00179-2

Task 2 – Conduct Integrated Cost-Benefit Analysis of Impacts of Naphthalene Removal in the United States

Massachusetts Institute of Technology

Objective

The objective of this Task is to produce an integrated cost-benefit analysis of naphthalene removal in the United States, accounting for the additional refining cost as well as the air quality and climate impacts.

Research Approach

The overall cost-benefit assessment of naphthalene removal includes fuel production costs, air quality benefits, and climate impacts from fuel production and fuel consumption. Fuel production costs were evaluated in tasks that were completed in previous project years. Air quality benefits and non-contrail climate impacts were calculated per unit reduction in nvPM mass and number emissions, based on the results of Grobler et al. (2019). These impacts are then scaled using the emissions reductions determined in the results of Task 1. Contrail impacts are estimated based on contrail modeling studies which investigated the effect of reductions in the soot number EI (Caiazzo et al., 2017; Bier & Burkhardt, 2019). Finally, all effects are placed on a common monetized basis to compare different naphthalene removal scenarios. We consider uncertainties in the assessment of each component and use these uncertainties to compute the likelihood of a net benefit for different scenarios.

Milestone

The work completed for this Task was presented at the Aviation Emissions Characterization (AEC) Roadmap annual meeting in May 2020.

Major Accomplishments

The processing costs, air quality benefits, and climate impacts of naphthalene removal are converted to a common basis of cents per liter, as presented in Table 1. The benefits of widespread naphthalene removal are outweighed by the costs of processing the fuel and the CO_2 emissions associated with that processing.

Table 1. Costs (positive) and benefits (negative) of naphthalene removal.

	Component	Hydrotreatment (¢/liter)		Extractive Distillation (¢/liter)	
		Median	95% CI	Median	95% CI
Processing	Refinery	2.4	2.0 – 2.7	1.7	1.5 – 2.0
Air quality	nvPM	-0.004	0 – -0.01	-0.009	0 – -0.03
	Fuel sulfur	-0.51	-0.28 – -0.73	0	
Climate	nvPM	-0.02	0 – -0.04	-0.04	-0.01 – -0.09
	Fuel sulfur	1.06	0.15 – 2.85	0	
	Contrails	-0.16	-0.04 – -0.44	-0.38	-0.09 – -1.0
	Refinery CO_2	0.46	0.08 – 1.19	0.48	0.08 – 1.27
Total		**3.2**	**2.2 – 4.7**	**1.8**	**1.0 – 2.5**

For hydrotreatment, the climate impacts of the refinery CO_2 emissions exceed the expected air quality and climate benefits associated with the reduction in soot emissions. Furthermore, the net present value (NPV) of the climate warming associated with sulfur removal is greater than the NPV of the reduced air-quality-related damages. For extractive distillation, the median air quality and climate benefits are approximately equal to the societal cost of the refinery CO_2 emissions. In addition to these environmental costs, the costs associated with processing jet fuel in the refinery must also be considered. These results suggest that, in the absence of a strong contrail effect, naphthalene removal on a nationwide basis is unlikely to be cost beneficial using either extractive distillation or hydrotreatment. However, it may be possible that naphthalene removal could be beneficial under certain circumstances, e.g., if applied to fuels used at individual airports with particular air quality concerns, or if used at times in locations where the formation of net warming contrails is most likely.

Publications
N/A

Outreach Efforts
The results of this work were presented at the Aviation Emissions Characterization (AEC) Roadmap annual meeting held in May 2020.

Awards
None

Student Involvement
This task was conducted primarily by Drew Weibel, working directly with Prof. Steven Barrett and Dr. Raymond Speth. Mr. Weibel graduated with a Master of Science in 2018.

Plans for Next Period
Task is complete.

References
Bier, A., & Burkhardt, U. (2019). Variability in Contrail Ice Nucleation and Its Dependence on Soot Number Emissions. *Journal of Geophysical Research: Atmospheres*, *124*(6), 3384–3400. https://doi.org/10.1029/2018JD029155

Caiazzo, F., Agarwal, A., Speth, R. L., & Barrett, S. R. H. (2017). Impact of biofuels on contrail warming. *Environmental Research Letters*, *12*(11), 114013. https://doi.org/10.1088/1748-9326/aa893b

Grobler, C., Wolfe, P. J., Dasadhikari, K., Dedoussi, I. C., Allroggen, F., Speth, R. L., Eastham, S. D., Agarwal, A., Staples, M. D., Sabnis, J., & Barrett, S. R. H. (2019). Marginal climate and air quality costs of aviation emissions. *Environmental Research Letters*, *14*(11), 114031. https://doi.org/10.1088/1748-9326/ab4942